



HAL
open science

Seismicity Controlled by a Frictional Afterslip During a Small-Magnitude Seismic Sequence (M L

Alexandre Canitano, Maxime Godano, Ya-Ju Hsu, Hsin-Ming Lee, Alan Linde, Selwyn Sacks

► **To cite this version:**

Alexandre Canitano, Maxime Godano, Ya-Ju Hsu, Hsin-Ming Lee, Alan Linde, et al.. Seismicity Controlled by a Frictional Afterslip During a Small-Magnitude Seismic Sequence (M L

HAL Id: hal-01856082

<https://hal.science/hal-01856082>

Submitted on 1 Dec 2021

HAL is a multi-disciplinary open access archive for the deposit and dissemination of scientific research documents, whether they are published or not. The documents may come from teaching and research institutions in France or abroad, or from public or private research centers.

L'archive ouverte pluridisciplinaire **HAL**, est destinée au dépôt et à la diffusion de documents scientifiques de niveau recherche, publiés ou non, émanant des établissements d'enseignement et de recherche français ou étrangers, des laboratoires publics ou privés.

Copyright

RESEARCH ARTICLE

10.1002/2017JB015128

Key Points:

- We present a rare observation of seismic-aseismic fault coupling during a small-magnitude seismic sequence ($M < 5$)
- We show that the cumulative aseismic moment of the postseismic phase is at least equivalent to the coseismic moment of the sequence
- We estimate the frictional properties of the Chihshang Fault using the volumetric strain signal recorded during a shallow afterslip

Supporting Information:

- Supporting Information S1
- Data Set S1
- Data Set S2

Correspondence to:

A. Canitano,
canitano@earth.sinica.edu.tw

Citation:

Canitano, A., Godano, M., Hsu, Y.-J., Lee, H.-M., Linde, A. T., & Sacks, S. (2018). Seismicity controlled by a frictional afterslip during a small-magnitude seismic sequence ($M_L < 5$) on the Chihshang Fault, Taiwan. *Journal of Geophysical Research: Solid Earth*, 123, 2003–2018. <https://doi.org/10.1002/2017JB015128>

Received 19 OCT 2017

Accepted 4 FEB 2018

Accepted article online 9 FEB 2018

Published online 28 FEB 2018

Seismicity Controlled by a Frictional Afterslip During a Small-Magnitude Seismic Sequence ($M_L < 5$) on the Chihshang Fault, Taiwan

Alexandre Canitano¹ , Maxime Godano², Ya-Ju Hsu¹ , Hsin-Ming Lee¹, Alan T. Linde³, and Selwyn Sacks³

¹Institute of Earth Sciences, Academia Sinica, Taipei, Taiwan, ²Université Côte d'Azur, CNRS, Observatoire de la Côte d'Azur, IRD, Géoazur, Valbonne, France, ³Department of Terrestrial Magnetism, Carnegie Institution of Washington, Washington, DC, USA

Abstract We report evidence for frictional afterslip at shallow depths (about 5 to 7 km) during a small-magnitude seismic sequence (with $M_L < 5$) along the Chihshang Fault, a main active structure of the Longitudinal Valley, in southeast Taiwan. The afterslip, which was recorded by a nearby borehole dilatometer, lasted about a month with a cumulative geodetic moment magnitude of 4.8 ± 0.2 . The afterslip comprised two stages and controlled the aftershock sequence. The first postseismic stage, which followed a M_L 4.6 earthquake, lasted about 6 h and mostly controlled the ruptures of neighboring asperities (e.g., multiplets) near the hypocenter. Then, a 4 week duration large afterslip event following a M_L 4.9 earthquake controlled the rate of aftershocks during its first 2 days through brittle creep. The study presents a rare case of simultaneous seismological and geodetic observations for afterslip following earthquakes with magnitude lower than 5. Furthermore, the geodetic moment of the postseismic phase is at least equivalent to the coseismic moment of the sequence.

1. Introduction

Afterslip is a phase of postseismic relaxation for moderate to large earthquakes ($M > 6$) and occurs on the fault plane in response to the stress change imparted by a coseismic stress drop (e.g., Bürgmann et al., 2002; Hsu et al., 2007; Marone et al., 1991; Perfettini & Avouac, 2004). Afterslip often occurs in regions surrounding the coseismic slip zone, where the coseismic static stress variations are large, and thus releases accumulated strain at shallow depths (D'Agostino et al., 2012; Hsu et al., 2006; Mahsas et al., 2008; Wei, Barbot, et al., 2015). Postseismic slip following large earthquakes has long been documented in a variety of tectonic events, and its spatial distribution is often complementary with the coseismic slip (Mendoza & Hartzell, 1988). In general, for $M > 6$ earthquakes, the moment of the cumulative postseismic slip represents only a small portion of the coseismic moment (e.g., D'Agostino et al., 2012; Hsu et al., 2006; Johanson & Bürgmann, 2010); however, some rare cases show the postseismic moment similar or larger than the coseismic moment (Freed, 2007; Langbein et al., 2006). More rarely, for large earthquakes, it has been observed that aftershocks may be controlled by the stressing rate associated with afterslip (Hsu et al., 2006; Perfettini & Avouac, 2004, 2007; Perfettini et al., 2005).

Observations of postseismic phase following smaller earthquakes ($M < 6$) remain rare. For instance, interferometric synthetic aperture radar data allowed detection of aseismic creep with geodetic moment of about 6 triggered by a pair of M_w 5.9 earthquakes in the Zagros Mountains of Iran (Barnhart & Lohman, 2013), as well as afterslip following the 2007 M_w 5.5 Ghazaband earthquake, Pakistan, which released about 70% of the moment of the main event (Fattahi et al., 2015). Interferometric synthetic aperture radar data also revealed a slow postseismic phase with magnitude larger than 5 associated with the M 4.7 2008 Reno-Mogul earthquake (Bell et al., 2012) and afterslip with geodetic magnitude of 5.5 and with duration of about 1 year following a M_w 5 shock in Afghanistan (Furuya & Satyabala, 2008). Moreover, afterslip lasting a few hours and releasing almost the same amount of slip of the 1997 Aichiken-Tobu earthquake (M_w 5.7) in Japan has also been observed on strainmeter data (Takai et al., 1999). In general, the moment of postseismic slip for small earthquakes is about the same order of magnitude, or even larger, than the coseismic moment (Fattahi et al., 2015; Hawthorne et al., 2016). This feature has also been evidenced on strainmeter signals for multiple M 1.9–5 earthquakes near San Juan Bautista, California (Hawthorne et al., 2016). Small to large earthquakes may exhibit

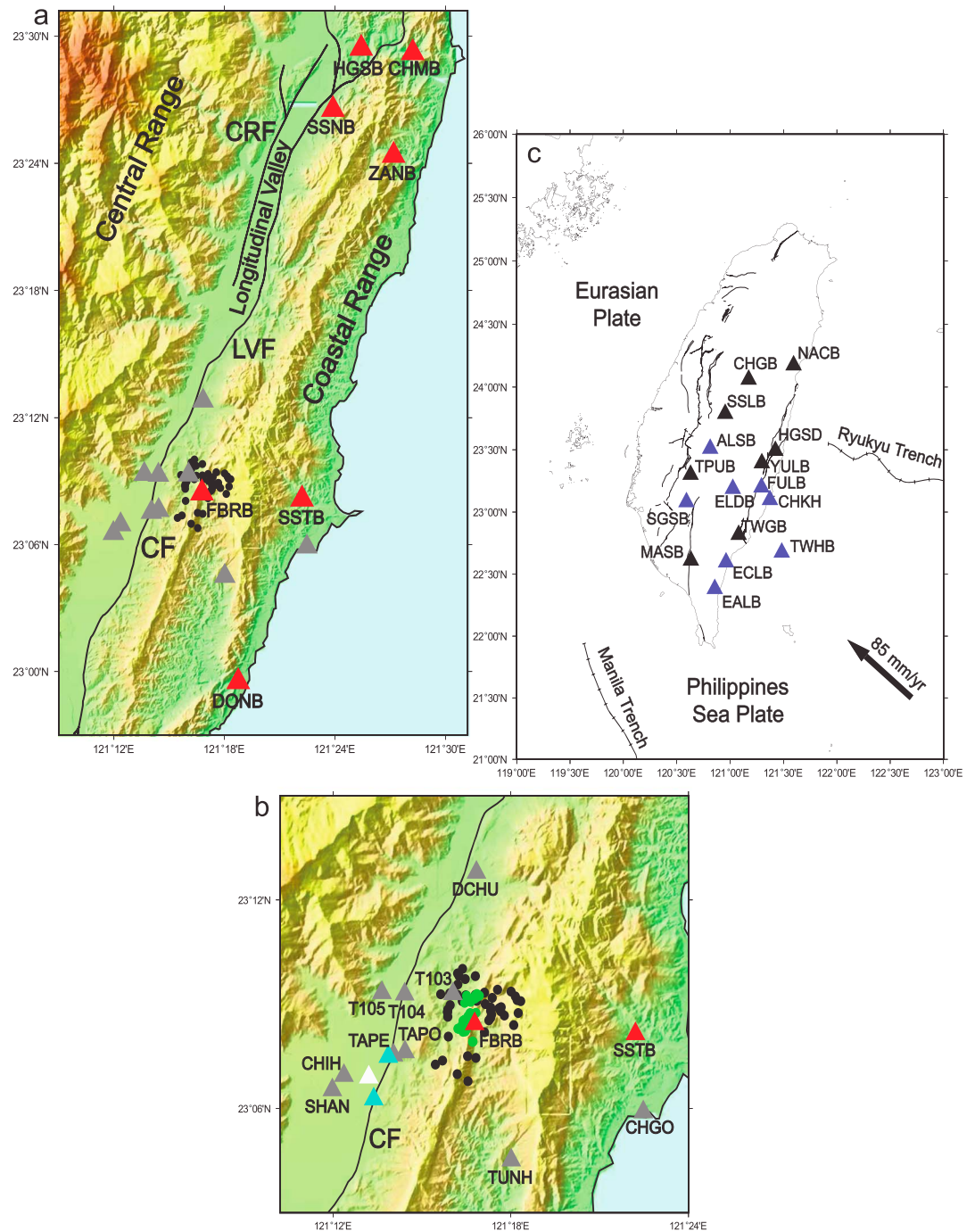


Figure 1. (a) Main structures in eastern Taiwan (LVF = Longitudinal Valley fault; CRF = Central Range fault; CF = Chihshang Fault). Black dots show seismicity from 12 to 15 April 2010. Red and gray triangles denote the dilatometers and Global Positioning System (GPS) stations, respectively. (b) Zoom on the seismic sequence occurring on the CF near FBRB dilatometer. Green dots show relocated seismicity (section 4.1). Light blue and white triangles denote the two creepmeters and meteorological site COS740 operated by the Central Weather Bureau of Taiwan, respectively. (c) Geodynamic framework of Taiwan. Black arrow indicates relative motion between Philippine Sea plate and Eurasian plate. Black and blue triangles denote broadband seismometers operated by the Institute of Earth Sciences (IES) (Broadband Array in Taiwan for Seismology network, BATS) and by the Central Weather Bureau (CWB) used in this study, respectively.

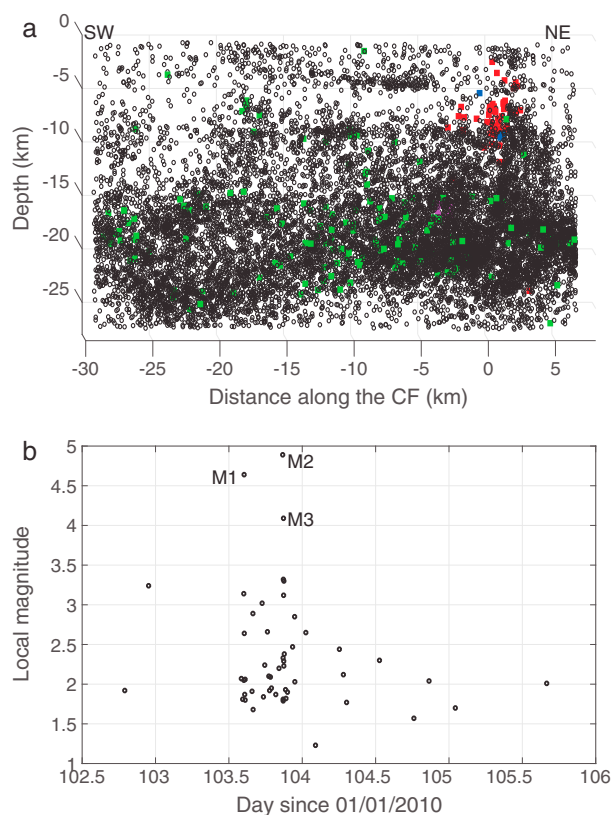


Figure 2. (a) Seismicity over the past two decades (from 1993 to 2014 with $M_L \geq 1.5$) (black dots) on the Chihshang Fault (CF; SW-NE view). Green squares denote the events with $M_L > 4$. Red squares denote the earthquakes considered in the study. The three mainshocks ($M_L \geq 4$) are depicted by blue squares. Magenta square denotes the hypocenter of the 2003 M_w 6.8 Chengkung earthquake. The present seismic sequence is located at the NE termination of the 2003 Chengkung earthquake rupture. Origin for distance axis is the latitude of FBRB dilatometer. (b) Magnitude distribution of the earthquakes during the sequence (13 to 15 April 2010). Event M2 occurred 6 h after M1.

common slip transient in postseismic phase and postseismic deformation associated with a small-magnitude earthquake sequence can thus significantly contribute to the energy budget of earthquakes. Therefore, the analysis of postseismic phases for small earthquakes is important for earthquake hazard but the detection remains challenging.

We report new evidence for the detection of postseismic deformation associated with a $M_L < 5$ earthquake sequence that occurred on 13 to 15 April 2010 on the Chihshang Fault (CF). Afterslip has been recorded by a nearby borehole dilatometer, and lasted about a month, with a cumulative geodetic moment magnitude of 4.8 ± 0.2 . The CF is located in the middle section of the Longitudinal Valley Fault (LVF) (Figure 1). The LVF is considered as a plate boundary between the Eurasian and the Philippine Sea plates (Barrier & Angelier, 1986; Chai, 1972) and accounts for more than one third of the oblique plate convergence of about 85 mm/yr (Yu et al., 1997, 1999). The LVF is characterized by high rates of oblique slip on its southern segment and by primary left-lateral slip on its northern section (Shyu et al., 2005; Yu & Kuo, 2001). The listric SE dipping CF is the most active fault segment of the LVF (Angelier et al., 2000) with earthquake activity occurring mainly at depths between 10 and 25 km (Figure 2a) and dominated by reverse-type focal mechanisms (Kuoehen et al., 2004). Significant earthquakes have occurred on the CF in historic times, including the 1951 M_L 7.3 Taitung earthquake (Chen, Toda, & Rau, 2008) and the 2003 M_w 6.8 Chengkung earthquake (Ching et al., 2007; Hsu et al., 2009). Moreover, rapid shallow creep with the amplitude of 20–30 mm/yr has been evidenced by creepmeter monitoring (Lee et al., 2001, 2003, 2006) and geodesy (Champenois et al., 2012; Thomas, Avouac, Champenois, et al., 2014; Yu & Kuo, 2001). This shallow creep behavior has been found to be influenced by precipitation (Lee et al., 2003) and is modulated by the seasonal loading changes. The high rates of shallow creep on the fault are likely to be associated with the Lichi Mélange (Lee et al., 2001; Yu & Liu, 1989; Yu et al., 1997), a highly sheared mud unit with occasional coherent turbidite beds and exotic blocks of ophiolite and sedimentary rocks.

In this paper, we first present the geodetic (strainmeter and Global Positioning System, GPS) and seismological data recorded along the CF during April to May 2010 (section 2). We report afterslip and simultaneously ana-

alyze strain and seismicity using rate-dependent friction law to estimate frictional parameters of the CF (section 3). In section 4, we relocate and estimate the source parameters of the aftershocks and show evidence for repeater-type seismicity occurring during the sequence. We then estimate the cumulative geodetic moment magnitude of the sequence and discuss the seismic-aseismic coupling on the CF (section 5).

2. Data

2.1. Seismicity

The seismic sequence started on 13 April 2010 (day 103), lasted about 2 days, and occurred at a depth of about 5 to 10 km (Figure 2a, red squares) in a $\sim 5 \times 5$ km² area near the northeastern limit of the CF (Figure 1). The sequence was recorded by the seismic stations operated by the Central Weather Bureau (CWB) of Taiwan. The completeness of the Taiwan Earthquake Catalog catalog in the area for the period 2004–2010 is about 1.3–1.4 (Mignan et al., 2011), which corresponds to the lowest magnitude of the sequence. The sequence incorporates about 45 events with $M_L \sim 1.3$ –3.3 during about 2–2.5 days (Figure 2b). The sequence has been initiated by a M_L 4.6 earthquake (hereafter M1), followed 6–7 h later by a second shock of M_L 4.9 (M2). The seismicity following M1 is mostly earthquakes with small magnitude ($M_L \sim 1.6$ –3.1), while event M2 was followed by an aftershock with $M_L \sim 4.1$ (M3) about 6–7 min later and with nine events with $M_L \sim 2.5$ –3.3. The reported source parameters from the Broadband Array in Taiwan for Seismology (BATS) are (strike = 21°, dip = 59°, rake = 77°) for M1 and (strike = 27°, dip = 58°, rake = 81°) for M2. There was also a small preseismic

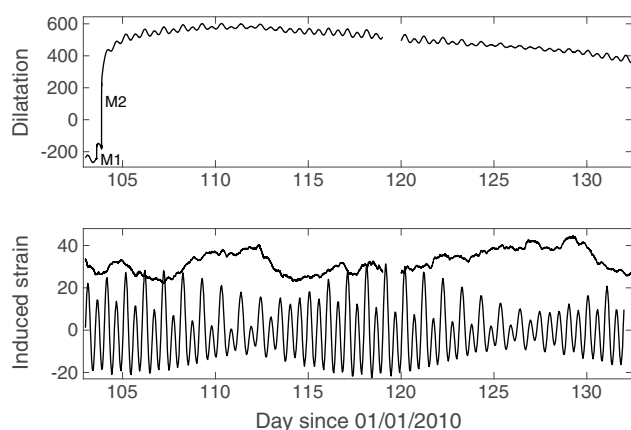


Figure 3. Signals at FBRB site (in $n\epsilon$) over a 1 month period (13 April to 12 May 2010). (top) Raw dilatation signal (expansion is positive). Labels M1 and M2 denote the coseismic static strain steps due to mainshocks M1 and M2, respectively. (bottom) Strain induced by air pressure (air pressure signal is detided) and by solid Earth and ocean tides.

Sacks-Evertson (Sacks et al., 1971) borehole strainmeters in southeast LV (see Figure 1a, sites FBRB, SSTB, and DONB). It was established to support GPS observations with the aim of detecting fault slip transients along the fault as well as to record the short- to long-term subsurface deformation. Strainmeters for continuous crustal strain monitoring are highly sensitive instruments with a precision better than 10^{-9} (i.e., less than 1 mm over a distance of 1,000 km) at a period $10^{-2} - 10^3$ s. Strainmeters established along the LVF allowed us to record and model relevant crustal signals such as large strain changes (a few hundred of nanostrain; $n\epsilon$) associated with typhoon passing (Hsu et al., 2015; Liu et al., 2009; Mouyen et al., 2017), coseismic static offsets (Canitano et al., 2015), near-field dynamic strain (Canitano et al., 2017), and tidal shear strain (Canitano et al., 2018).

FBRB dilatometer, which is installed at the depth of 200 m at a few kilometers east of the CF (Figure 1a), was the only instrument in the area that was in operation during the sequence (SSTB experienced a power outage and DONB was not installed). FBRB is calibrated against the Earth tides (M_2 constituent) by using the common technique of comparing output data with the modeled tidal signals (Hart et al., 1996). FBRB has nearly continuous records since its installation in 2008 (see Figure S1 in the supporting information). We processed the dilatation signal to remove a linear trend, the solid Earth, and ocean tidal strain (with *ETERNA 3.3* software; Wenzel, 1995) and the barometric pressure-induced strain ($-1.55 \pm 0.12 n\epsilon/\text{mbar}$). Note that the trend has been estimated using the 2 month data preceding the sequence (a contraction of about $-13.5 n\epsilon/\text{day}$) to avoid the bias due to the coseismic strain changes. The strain changes associated with the external perturbations are presented in Figure 3.

FBRB dilatometer also records long-term seasonal hydrologic variations of a few hundred of $n\epsilon$. They coincide with the shortening (about 1–2 mm) of the baseline between the closest GPS stations (see section S1 and Figure S2 in the supporting information for details). We processed GPS data with the *GAMIT10.42/GLOBK5.16* software packages (Herring et al., 2010) using the 2005 International Terrestrial Reference Frame (ITRF2005) (Altamini et al., 2007) coordinates in GLOBK processing. We also corrected GPS time series for common mode errors in the study area (see section S1 for additional details). Figure S3 in the supporting information shows the daily positions for east, north, and vertical components between March and May 2010.

3. Analysis and Modeling of Strain and Seismicity

3.1. Coseismic Deformation

FBRB dilatometer recorded a large expansion of about $10^3 n\epsilon$ over a 1 month period (April–May 2010, see Figure 3). Such a signal is unique in the strain records for the site. It differs from the usual large, compressive signals, resulting from large rain episodes typically associated with typhoons (a few $10^2 n\epsilon$) (see Figure S1). Note that no large rain episodes and no strong barometric changes occurred during the period of the study. Coseismic static offsets associated with M1 and M2 are both expansion with values of about $80 n\epsilon$ and $325 n\epsilon$, respectively (Figure 4). Constraining the size of the fault planes remains difficult because of the scattered

sequence (six events with $M_L \sim 1.9 - 3.2$) that started on 12 April (day 102). Earthquakes are detailed in Table S1 in the supporting information.

The depths of the mainshocks (<10 km) contrast with most of the $M_L \geq 4$ events that occurred at depths greater than 10–15 km on the CF from 1992 to 2014 (Figure 2a, green squares). Only a few shallow earthquakes with $M_L \geq 4$ have been reported at depths above 10 km along the CF since 1992, and they predominantly occurred along the central to southwestern sections of the CF. Moreover, the sequence is located near the NE upper limit of the rupture area of the 2003 Chengkung earthquake (at the depth of about 10 km, see Figure 2a) in an area that experienced high postseismic slip (~ 10 cm) in the 5–6 months following the M_w 6.8 Chengkung earthquake (Hsu et al., 2009).

2.2. Geodesy

Continuous GPS stations have operated along the CF for more than a decade, together with rod-type creepmeters installed in 1998 (Lee et al., 2001). Beginning in 2007, the Institute of Earth Sciences (IES), Academia Sinica in cooperation with the Department of Terrestrial Magnetism, Carnegie Institution of Washington, has deployed a network of three

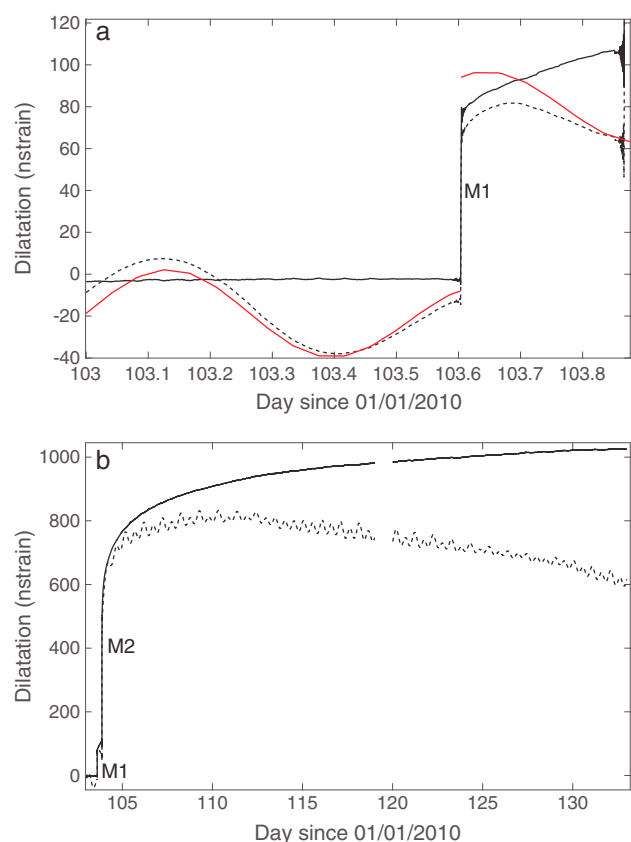


Figure 4. (a) Raw dilatation signal (dashed curve) and residual signal (solid curve) during 13 April 2010 (day 103) centered on mainshock M1 and depicting the initial stage of afterslip (stage A1) that reached a value of about $30 \text{ n}\epsilon$ after 6 h. The red curve denotes the predictions from solid Earth and ocean tidal model. (b) Large afterslip signal following earthquake M2 (stage A2) (solid curve) during a 1 month period. Dashed curve denotes the raw dilatation signal. The signal reached a value of about $600 \text{ n}\epsilon$ after a month and about 85% of the aseismic moment is released after a week. Labels M1 and M2 denote the coseismic static strain steps due to mainshocks M1 and M2, respectively.

starting immediately after M3 (which occurred about 6 min following M2), when the dilatation signal is more stable, depleted from the strain perturbation caused by the coseismic static step of M3 (with amplitude of about $20 \text{ n}\epsilon$) (see Figure S5a (inset) for details). Note that stage A2 results mostly from the contribution of event M2 (M_L 4.9), as event M3 (M_L 4.1) contribution could be neglected as the first-order approximation due to its smaller magnitude.

We see that the postseismic process of the sequence is mainly aseismic since there are no visible coseismic steps at the time of the aftershocks (excepted for M3). We also note that about 70% of the aseismic process (about $400 \text{ n}\epsilon$) is completed during the first 2 days. Aseismic events follow mostly a logarithmic decay function, with rapid slip occurring at the early stage of the process. After 1 week (day 111), about 85% of the aseismic moment of the afterslip has been released. Besides, afterslip did not appear in data collected at dilatometers in the central network (e.g., stations SSNB, HGSB, and ZANB), located about 40 km farther north. For these sites, a signal above the noise level at a few weeks period, which typically corresponds to $\sim 10\text{--}20 \text{ n}\epsilon$ (Canitano et al., 2013, 2014), would require a source with an aseismic moment magnitude larger than about 6.5.

3.3. Aftershocks Driven by a Frictional Afterslip

Comparing the seismicity during both afterslip stages (scaled on the 6 h duration of stage A1), we see that the cumulated number of aftershocks is slightly larger for stage A1 (18 and 13 events during stages A1 and A2, respectively), while the amplitude of strain transient is about 6 times larger for stage A2 (about $180 \text{ n}\epsilon$) (Figure 5). If we compare the cumulative number of aftershocks during stage A2, normalized by its value

distribution of the aftershocks. We thus estimate their dimensions and their coseismic slip using theoretical scaling laws (Kanamori & Anderson, 1975; Wells & Coppersmith, 1994) (see Text S2 for details). Considering a static dislocation in an elastic half-space (Okada, 1992) with the source parameters described above, we see that the static offsets are consistent with the seismic source parameters of events M1 and M2 when their fault planes are located between 6–8 km depth on the CF (see Text S2 and Figure S4). However, it is difficult to put tight constraints on the locations from solely the geodetic signals. Note that the GPS signals do not reveal any clear surface displacements larger than about 3–5 mm and 10 mm on the east/north and vertical directions, respectively (see Figure S3). Moreover, no clear signal has been detected by the two nearby creepmeters located SW of the sequence (Figure 1b, light blue triangles).

3.2. Postseismic Deformation

Processed data show a small amplitude expansive signal starting after event M1 (Figure 4a). The latter is also particularly obvious when we compare the raw signal (dashed curve on Figure 4a) with its solid Earth and ocean tidal model (red curve). Before the coseismic step of M1 the discrepancy between the raw signal and the tidal model is $\sim 3 \text{ n}\epsilon$, while instantaneously following the earthquake, there is a difference of about $25 \text{ n}\epsilon$. The discrepancy is not due neither to any residual atmospheric change (it would correspond to a pressure decrease of about 16 mbar within a few minutes) nor to rain (which would produce a contraction). The slow afterslip phase reaches a value of about $30 \text{ n}\epsilon$ in about 6 h (i.e., the duration until M2 occurs). Following earthquake M2, the dilatation signal exhibits a large afterslip phase of about $600 \text{ n}\epsilon$ over 4 weeks.

In the following, we consider two main stages of afterslip, described as follows:

1. Stage A1: the 6 h length signal initiated by earthquake M1, which occurred between mainshocks M1 and M2 and reached an amplitude of about $30 \text{ n}\epsilon$ (Figure 4a).
2. Stage A2: the large afterslip signal following M2, which lasted about 4 weeks with a cumulative strain change of about $600 \text{ n}\epsilon$ (i.e., 20 times the amplitude level reached by stage A1) (Figure 4b). However, for the following analysis, we referred to as “stage A2,” the part of the signal

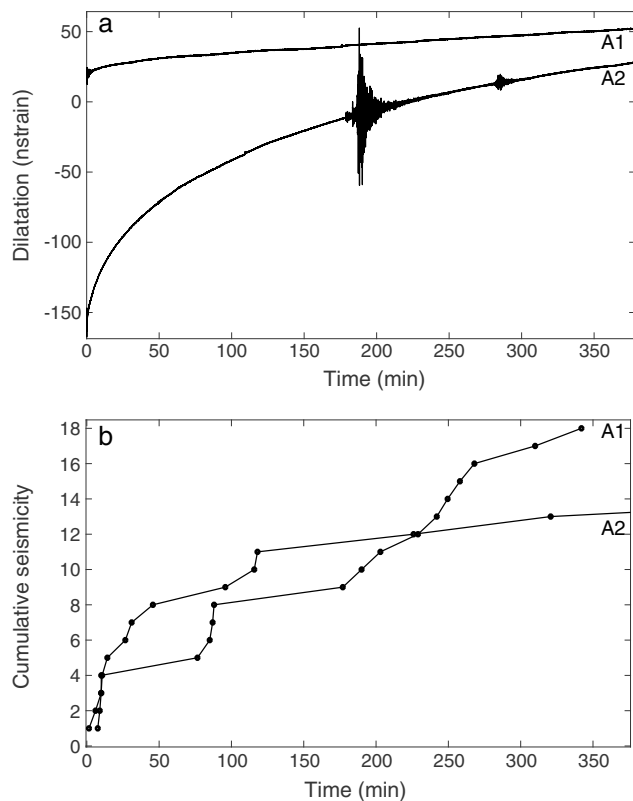


Figure 5. (a) Evolution of afterslip and (b) cumulative seismicity. Both evolutions are scaled on the 6 h duration of stage A1. The cumulative seismicity during the first 6 h of evolution of each phase is slightly larger for stage A1 (about 18 and 13 events during stages A1 and A2, respectively), while the amplitude of strain transient is about 6 times larger for stage A2 than that for stage A1 (about 180 $n\epsilon$). See section 2.1 and Table S1 in the supporting information for details about seismicity.

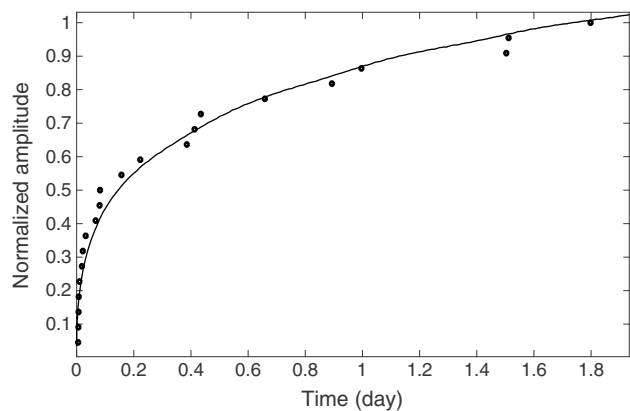


Figure 6. Comparison of the evolution of the cumulative number of aftershocks (solid dots) (with $M_L > 1.3$) with the afterslip signal over the first 2 days of stage A2 (solid curve). Cumulative seismicity and dilatation have been normalized by their maximal amplitude after 2 days (i.e., about 22 earthquakes and about 347 $n\epsilon$, respectively). About 50% of the aftershocks (22 events over 45) appear to be driven primarily by the early afterslip.

at the end of the seismic sequence (i.e., after about 2 days), with the normalized strain signal during the same period of stage A2, it appears that the cumulative number of aftershocks is proportional to the strain change during the early stage of afterslip (Figure 6). This appears to be the evidence for seismicity driven primarily by the large afterslip phase. Note that such a dependence is not evidenced neither for the afterslip phase between M2 and M3 (Figure S5b) nor for stage A1 (Figure S6). The stress change of the early postseismic stage A2 is fast; therefore, it may eventually be capable of triggering more events that are close to critical conditions.

3.4. Fault Zone Frictional Properties

Assuming that afterslip results from rate-strengthening frictional sliding on the fault plane in response to the coseismic stress change imparted by a mainshock, we can model aseismic creep through a rate-dependent friction law (Perfettini & Avouac, 2004). We model the temporal evolution of strain and seismicity for stage A2 only, as stage A1 duration is probably too short to allow for a robust modeling. The temporal evolution of the dilatation signal $\epsilon_a(t)$ during stage A2 can be stated as follows:

$$\epsilon_a(t) = \epsilon_0 t_r \log(1 + d(\exp(t/t_r) - 1)) \quad (1)$$

where ϵ_0 is the volumetric long-term strain rate, $t_r = A\sigma_n/\dot{\tau}$ is the relaxation time, and $d = \exp(\Delta\sigma/A\sigma_n)$ (σ_n is the normal stress, A is a rheological parameter, and $\dot{\tau}$ the interseismic shear stress) is the velocity jump due to the coseismic shear stress change $\Delta\sigma$ on the fault (Perfettini & Avouac, 2004). Furthermore, if aftershock productivity is controlled by the stressing rate associated with afterslip, it implies that both processes should have the same temporal evolution (i.e., the same time constant). Therefore, the cumulative number of earthquakes $R(t)$ during stage A2 should be of the form (Perfettini & Avouac, 2004):

$$R(t) = R_0 t_r \log(1 + d(\exp(t/t_r) - 1)) \quad (2)$$

where R_0 is the background seismicity rate during interseismic stress buildup.

By trial and error, we achieved a good fit for the dilatation signal of stage A2 during its first 2 weeks (Figure 7a, vertical dashed line), which covers about 85–90% of the amplitude of strain transient. The inferred values show $t_r \sim 35$ days, $d \sim 10^3$, and $\epsilon_0 t_r \sim 192$. We derive the value $\epsilon_0 \sim 2 \times 10^3 n\epsilon \text{ yr}^{-1}$, which is consistent with the areal strain value derived from GPS signals (about a few $10^3 n\epsilon \text{ yr}^{-1}$) (Hsu et al., 2012). Moreover, cumulative seismicity over 2 days following stage A2 can be fitted with the same parameters (Figure 7b). From equation (2) we derive a value of $\epsilon_0 t_r \sim 4.7$. This corresponds to $R_0 \sim 50$ events/yr (with $M_L > 1.3$) during interseismic stress buildup, in good agreement with the low seismicity rate in the area (a few tens of events per year).

The location of M2 is not well resolved; however, values inferred from geodesy (see section S2 in the supporting information) and from earthquake relocation (see section 4.1 and Figure 8, orange star) are consistent (i.e., a focal depth of about 6.5–7 km). We compute the coseismic shear stress change for M2 at the depth of 6.5 km using *Coulomb 3.4* (Lin & Stein, 2004; Toda et al., 2005). We retained a mean value $\Delta\sigma \sim 0.2$ MPa (2 bar) at a distance of about 1–2 km from the fault plane (see Figure S7). The parameters resulting from our best fitting model and equation (1) allow us to derive a value of $A\sigma_n$ of about 0.03 MPa. This value is on the lower bound of the range derived from previous studies along the CF (~ 0.03 –0.5 MPa)

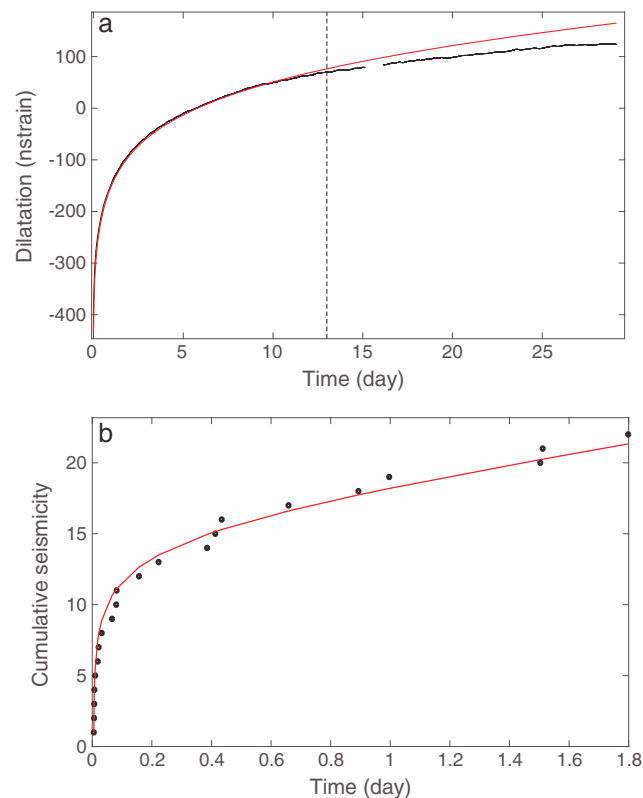


Figure 7. (a) Dilatation signal for stage A2 (black curve) and fit with a rate-dependent frictional model (red curve) (equation (1)) over a 1 month period. (b) Cumulative number of aftershocks (black dots) during the first 2 days of evolution of stage A2 and fit with a rate-dependent frictional model (red curve) (equation (2)). The dashed vertical line denotes the limit (first 13 days) for a satisfactory fit between observations and model predictions that covers about 85–90% of the afterslip evolution. The inferred parameters for both models show $t_r \sim 35$ days, $d \sim 10^3$, $e_0 t_r \sim 192$, and $R_0 t_r \sim 4.7$.

(Hsu et al., 2009). If we assume the effective normal stress σ_n of about 100 MPa at 6–7 km depth, A is about 3×10^{-4} that is consistent with values derived from other afterslip models for megathrust earthquakes (Hsu et al., 2006; Johnson et al., 2006) and for the 2003 Chengkung event ($A \sim 3 \times 10^{-4} - 5 \times 10^{-3}$) (Hsu et al., 2009). An estimate of the interseismic shear stress rate $\dot{\tau} (= A\sigma_n/t_r)$ leads to a value of about 0.3 MPa yr⁻¹ that is about 7.5 times larger than a previous estimate from 6 month duration GPS data (about 0.04 MPa yr⁻¹) (Hsu et al., 2009). The discrepancy may be due to errors in extrapolating the time constant of our short-duration afterslip observation (1 month). It may also come from an overestimation of M2 coseismic shear stress $\Delta\sigma$ that yields an overestimation of $A\sigma_n$ parameter.

4. Analysis of the Aftershocks

4.1. Relocation

We analyze the 100 Hz sampling seismic data recorded at 16 broadband stations, located at distance ranging from about 6 to 100 km from the seismic sequence (see Figure 1c). We examine events with sufficient signal-to-noise ratio (SNR) for the vertical component to allow picking the wave arrivals at the stations. The seismicity is relocated using the double-difference algorithm *HypoDD* (Waldhauser & Ellsworth, 2000) with manually picked *P* wave and *S* wave absolute arrival times and relative *P* wave delay times. Signals are filtered between 1 and 15 Hz to suppress microseismic noise, and we compare cross-correlation coefficients of the vertical components for all earthquake pairs for each station. The cross-correlation window has a length of 1.5 s and begins 0.1 s before manual *P* wave pick. In order to increase the precision of delay time measurement, the cross-correlation function is resampled with a resolution of 1 ms using Wiggins' weighted average-slopes interpolation method (implemented in Seismic Analysis Code). As our study involves few correlations, we consider that two earthquakes belong to the same cluster if the correlation coefficient (cc) is greater than 0.70 for the vertical component at least at two stations.

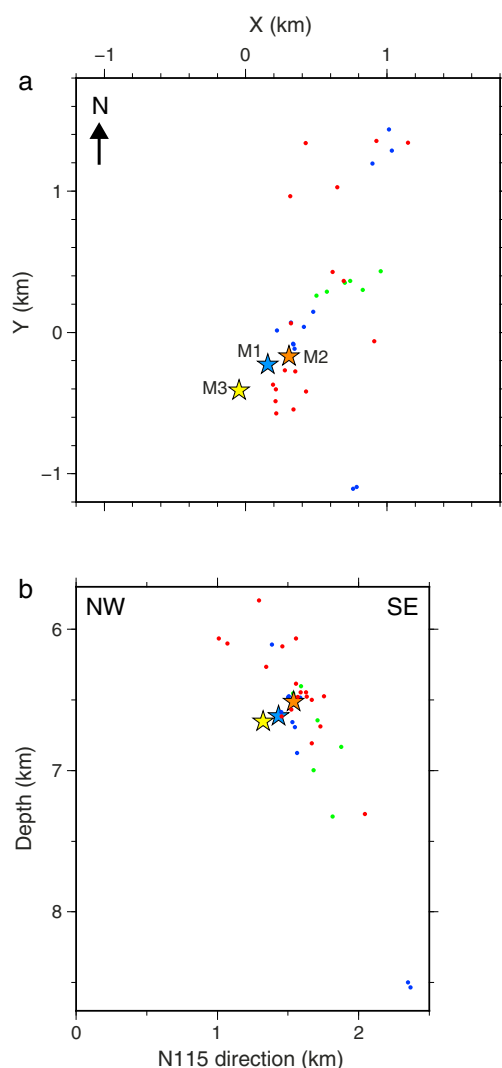


Figure 8. Double-difference relocation of the seismicity. (a) Longitude-latitude (X - Y) map of the relocated seismicity. Mainshocks are depicted by stars (M1: blue star, M2: orange star, and M3: yellow star), and aftershocks are depicted by dots (green dots: events occurring before M1, blue dots: events occurring between M1 and M2, and red dots: events occurring after M2). (b) A cross section along $N115^\circ E$. Seismicity is located at the depth of 6–7 km approximately on a $\sim 60^\circ$ SE dipping plane and is compatible with the geometry of the CF.

As a result, 39 earthquakes (3 mainshocks and 36 aftershocks) are relocated inside a NE-SW elongated cluster dipping southeastward ($\sim 60^\circ$) between 6 and 7 km at depth (Figure 8). Following Waldhauser and Ellsworth (2000), relative location uncertainties are assessed by a bootstrap resampling method. The P wave and S wave delay times obtained from manual picks and cross correlations are replaced by samples drawn in the residual time distributions given by the double-difference relocations. These samples are next relocated that allows us to determine the shift location related to the residual times. The process is repeated 200 times, and the distribution of the cumulative results (200×39 points) gives an estimation of the relative uncertainties (Figure S8 in the supporting information). We thus obtain horizontal and vertical relative uncertainties of about 50 m and 100 m, respectively. Projection of the relocated seismicity on the CF fault plane shows that aftershocks are located in a ~ 2 km \times 1.5 km area extending to the northeast of the hypocenters of mainshocks (Figure 9a). While seismicity following M1 (blue dots) is clustered in a 2 km long and 0.4 km wide zone (see Figures 9b and 9c), seismicity following M2 seems to migrate mainly in the updip direction (about 0.7–1 km within a few hours; see Figures 9b and 9c, red dots). This may correspond to a migration with a mean velocity of roughly 0.1 km/h, close to velocities of 0.1–1 km/h as observed for earthquake swarms driven by creep (Lohman & McGuire, 2007; Roland & McGuire, 2009). Nevertheless, eventual migration of seismicity is difficult to interpret due to the paucity of earthquakes during the sequence and due to its short duration (about 2 days).

4.2. Source Parameters

The source parameters of the relocated earthquakes (magnitude, rupture size, coseismic slip, and static stress drop) are estimated following the method proposed by Godano et al. (2015). This consists on a Bayesian inversion of the displacement spectral ratios between all the possible pairs of nearby located earthquakes. The use of spectral ratios suppresses the spectral contribution of propagation and site effects that can be considered nearly identical for tight clusters. This approach provides estimates of the scalar seismic moment (M_0), the P wave and S wave corner frequencies (f_{c_p} and f_{c_s}), and their associated uncertainties. The sampling rate of the signals is 100 Hz; hence, spectra are computed up to 50 Hz. However, to ensure that high-frequency part of spectra is not distorted by the anti-alias filter deployed in analog-to-digital converters, we consider only a frequency range below 40 Hz for the computation. Next, SNR is computed by taking the mean of the ratio between P and S spectrum and the spectrum of a noise window taken before the P wave. Finally, P and S spectral ratios for event pairs having displacement spectra with SNR greater than

1.5 are computed at each station. As a result, f_{c_p}/f_{c_s} ratios vary between 1 and 1.5 for most of the events (Figure S9 in the supporting information), which may indicate circular cracks as demonstrated by mechanical models (e.g., Madariaga, 1976).

We calculate earthquake magnitude, stress drop, and rupture size in the case of circular ruptures as suggested by previous estimates of f_{c_p}/f_{c_s} ratios. Details about the method are given in section S3 in the supporting information. Figure 10a displays the scaling law between magnitude and rupture size for 39 earthquakes. Source parameters are given in Table S3 in the supporting information. The moment magnitude distribution of the events lies in the range 1.7–4.4. Source radii are ranging from 40 to 200 m with uncertainties of about 15 to 100 m. Static stress drop varies between 5 and 50 MPa for small earthquakes ($M_0 < 10^{15}$ N m) and seems to be independent of the size and magnitude of the events. The lowest magnitude events ($M_0 < 10^{12}$ N m) also deviate from the constant stress drop trend and have a constant source radius (~ 30 –40 m). This effect is related to the maximum frequency of about 40 Hz considered in the spectral ratio inversion that excludes estimated source radii lower than about 30–40 m. The three mainshocks ($M_0 > 10^{15}$ N m) have a static stress

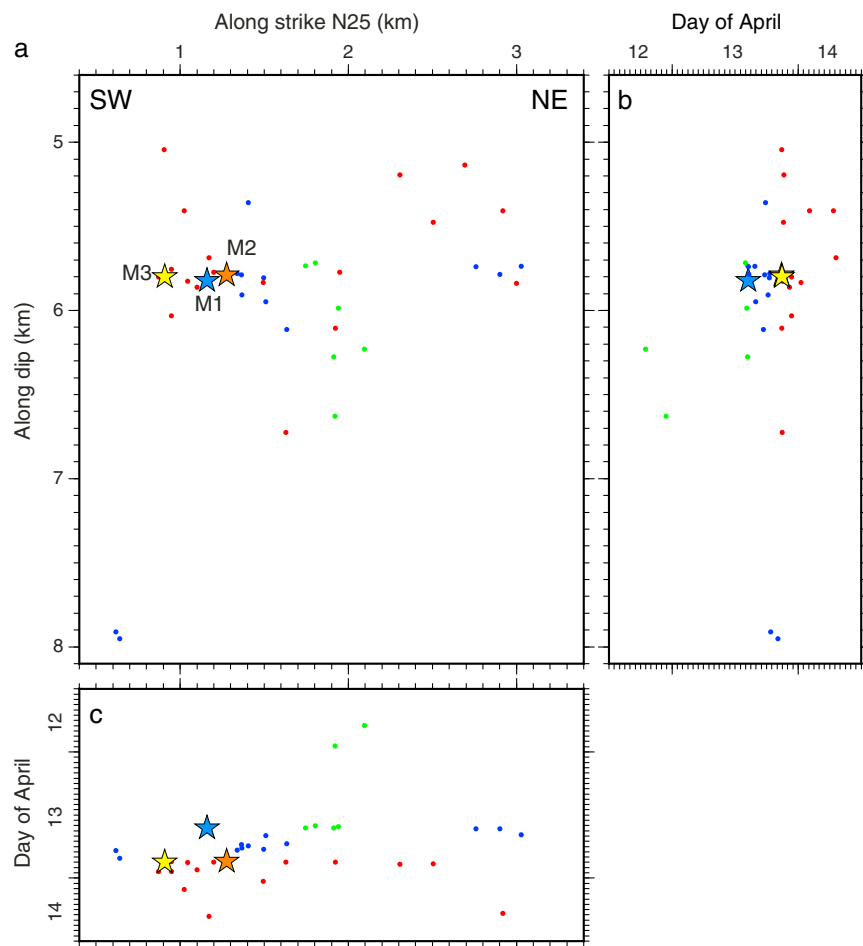


Figure 9. (a) Projection of the relocated seismicity on the CF fault plane (strike = 25° and dip = 60°). Seismicity is located in an area of about 2 km × 1.5 km on the CF (see Figure 8 for earthquake details). Temporal evolution of the seismicity (b) along dip and (c) along strike during 12 to 14 April 2010.

drop roughly ranging between 100 and 370 MPa that deviates from a constant stress drop trend of 5–50 MPa. However, stress drop uncertainties for the three mainshocks are large (between 90 and 310 MPa), with error bars overlapping the 50 MPa constant stress drop curve. These large uncertainties and apparent deviation from a constant stress drop could be explained by the inaccuracy of circular source model. Indeed, for these three larger earthquakes, rectangular fault geometry cannot be excluded (see Godano et al., 2015 for details) but has not been considered as we are mostly interested in microearthquake source parameters. Figure 10b displays the patch of the CF plane that seismically ruptured during the sequence. The projection onto the fault plane of the centroid and rupture surface of each earthquake shows the source overlapping is rather limited, excepted for a small area (about 1 km²) that encompasses the mainshocks (Figure 10b, dashed box) and also exhibits nearly repeated ruptures. We further detail the behavior of this area in the next section.

5. Discussion

5.1. Evidence for Nearly Identical Earthquakes in the Aftershock Sequence

Cross correlations of the aftershocks have revealed some highly correlated events. That concerns especially events F4-F7-F11, which show high waveform similitudes for most of the sites ($cc > 0.90$), even for remote stations (Figures 11a and 11b). Some other events, such as F10-F12-S17 and P3–P6, also show high similarity ($cc > 0.93$) but mostly for stations located near the sequence (less than about 30 km) (Figures 11c and 11d). Repeating earthquakes (REs) or multiplets are nearly identical seismic waveforms, diagnostic of the rupture of neighboring asperities (Igarashi et al., 2003; Taira et al., 2014; Turner et al., 2013; Vidale et al., 1994). They represent velocity-weakening regions that rupture repeatedly, their recurrence interval being determined

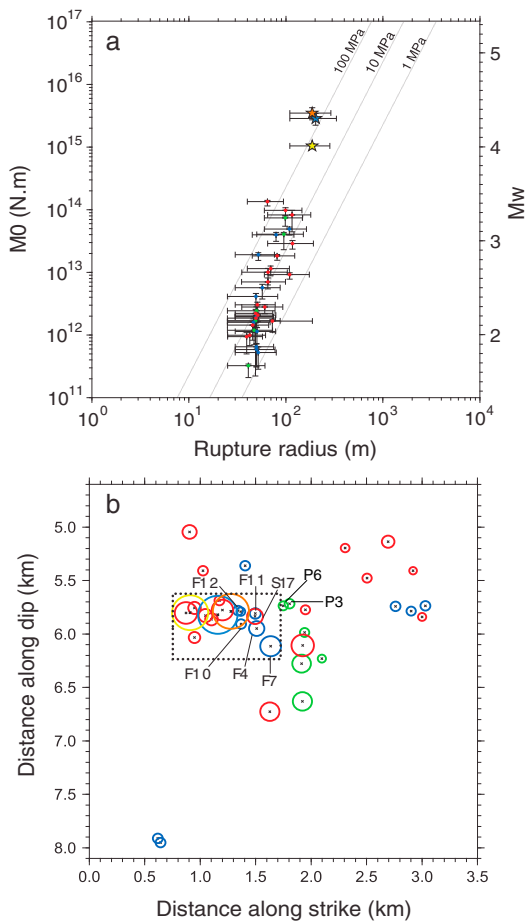


Figure 10. (a) Example of seismic scalar moment versus rupture radius at stations FULB (red), CHKH (green), ELDB (black), and YULB (blue) for the 39 earthquakes in the case of circular ruptures. Note that source parameters are calculated using the 16 stations. Stars denote mainshocks (see Figure 8 for details). Estimate of M_0 is directly made on the low-frequency part of displacement spectrum (plateau) that is taken as the mean of the displacement spectrum in the frequency band 1–3 Hz and next related to M_0 (Brune, 1970). (b) Projection of the centroid and rupture surface of each earthquake onto the CF plane (green circles, events occurring before M1; blue circles, events occurring between M1 and M2; and red circles, events occurring after M2). Dashed box depicts the area of multiple ruptures, and labeled events are the multiplets discussed in Section 5.

by the tectonic loading rate, while the surrounding velocity-strengthening region slips aseismically (Beeler et al., 2001; Nadeau & Johnson, 1998; Nadeau & McEvilly, 1999). REs have been observed along the northeastern section of the CF (Chen, Nadeau, & Rau, 2008; Chen et al., 2009), and they mainly occurred between depths of 12 and 20 km, in a region extending downdip to the present area. Only a few events occurred at shallow depth (above 8 km) during the past 15 years and some are located near the present sequence, at a distance of about 200–300 m. Chen et al. (2009) also reported that REs that occurred in this region have limited magnitude ($M_L < 3.5$) as do the events we infer here ($M_L \leq 3$). We however compared the events of the sequence with the reported REs but did not find any coherence between the signals.

Moreover, we also searched for additional events for the period 2004–2013 (about 80% of continuous data) using waveform similarity for each of the three groups of multiplets. Events F11, S17, and P3 are used as waveform templates for each group (see Figure 11). We performed sliding-window cross correlations (Yang et al., 2009) using each template at station FULB that has the highest SNR. We did not find any new event through this preliminary search to improve the relocations, as waveform similarities remain relatively low ($cc < 0.70$ for the vertical component). Therefore, some events may have escaped waveform detection or the recurrence interval of each sequence could be larger than the recurrence interval of the reported REs that ranges between 1 and 4 years (Chen et al., 2009). However, it has been shown that sequences of REs can also respond to nearby earthquakes with decreasing recurrence intervals (as burst-type repeaters) that are gradually recovering to preseismic rate, consistent with their being controlled by afterslip (Dominguez et al., 2016; Lengline & Marsan, 2009; Schaff et al., 1998; Uchida et al., 2003, 2015). This may suggest that the multiplets reported here, which occurred only during a few hours, have been activated by the afterslip (especially during stage A1) and therefore occurred exclusively during this sequence.

5.2. Nearly Repeated Ruptures Driven by Creep

In general, REs may act as a gauge for constraining preseismic or postseismic aseismic slip (Mavrommatis et al., 2015; Uchida et al., 2015); therefore, one can estimate aseismic slip based on the repeated ruptures of a single asperity. However, in this study, the resolution of the earthquake relocation and of their rupture radii are not robust enough to use them as “virtual creepmeters,” as the overlapping of the sources is rather limited (see Figure 10b). On the other hand, it is also possible that the image of the seismicity is as shown in Figure 10b (dashed box). The sequence is thus rather characterized by a few neighboring small asperities (with radius ~ 50 – 80 m), with sometimes partial overlapping (e.g., multiplets) located mostly in the northeastern edge and within the slip areas of the mainshocks.

Repeated ruptures of asperities within a few hours require a rapid reloading of the stress on the fault interface that is presumably a result of aseismic creep. Moreover, the large stress drop we infer for small earthquakes ($> \sim 5$ MPa) (see section 4.2) may suggest that repeating ruptures occurred at stuck asperities surrounded by an otherwise creeping fault plane as observed by Nadeau and Johnson (1998), for instance.

Repeater-type seismicity was found to occur days to months prior to large earthquakes (e.g., Kato et al., 2016; Ruiz et al., 2017), suggesting that a slow slip event may have preceded the rupture. We found REs occurring about 30 min to 3 min before M1 (events P3 and P6, see Figure 11d), which are located at the NE limit of the area of multiple ruptures described above (see Figure 10b) at the depth of about 6.5 km. This may suggest that a creep event preceded earthquake M1. Based on the repeated ruptures of multiplet P3–P6, the amount of aseismic slip associated with the slow event during about 30 min prior to M1 would be of ~ 1 cm (see Table S3 for details). However, no relevant strain signal larger than the noise level (a few 10^{-1} ϵ) was recorded by FBRB. To remain undetected shortly before M1, one aseismic source located near multiplet P3–P6

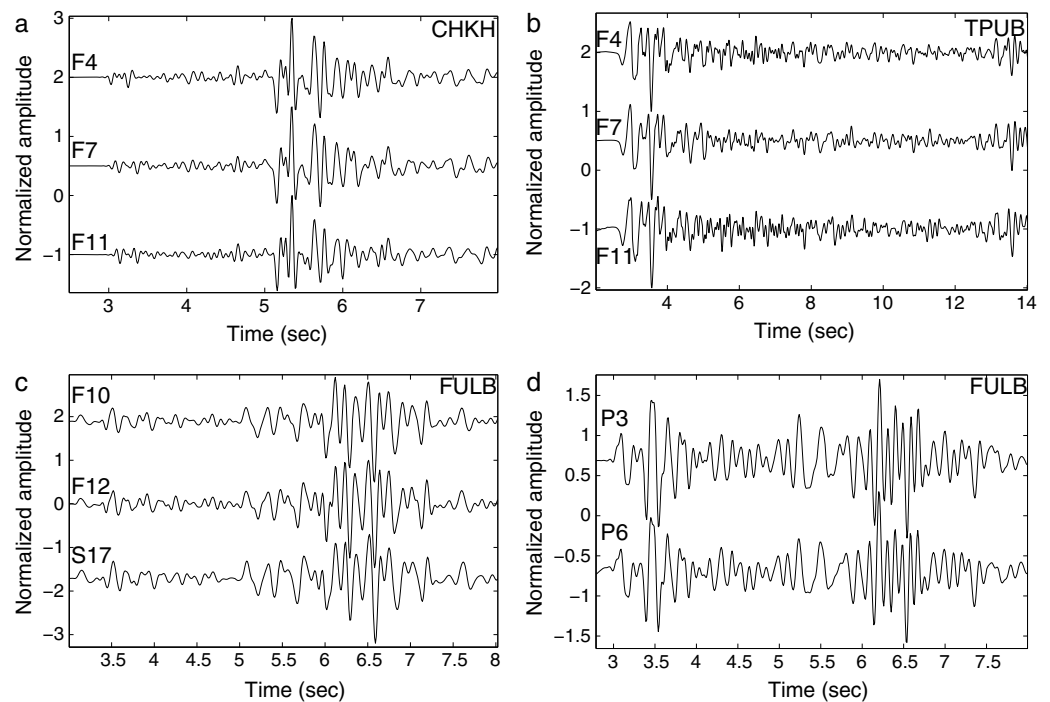


Figure 11. High waveform similarities (vertical component signals band passed between 1 and 15 Hz): (a) events F4-F7-F11 for station CHKH ($cc > 0.95$) and (b) station TPUB ($cc > 0.90$), (c) events F10-F12-S17 for station FULB ($cc > 0.96$) and (d) events P3-P6 for station FULB ($cc > 0.96$). Stations FULB, CHKH, and TPUB are located at distance of about 7 km, 10 km, and 70 km from the sequence, respectively. Events F11, S17, and P3 are used as templates for each group of multiplets (section 5.1).

would have dimensions roughly smaller than 1 km^2 (considering a slip value of about 1 cm) or equivalently would have characterized a geodetic moment magnitude lower than about 3.1.

5.3. Estimation of Aseismic Moment Magnitude With Geodesy

Based on a single geodetic observation and on the accuracy of previous estimates for aseismic slip, it remains difficult to constrain accurately the size and location of the source of afterslip. Besides, an additional complexity lies in the number of sources as the sequence is made of two stages. The existence of two distinct sources is suggested by the diversity of seismic processes during each stage. Indeed, while stage A2 controls the aftershock productivity during the first 2 days through slow shear failure (see Figure 6 for details), multiplets occurred mainly during the few hours of stage A1 (excepted event S17 and events P3-P6). On the other hand, the variability of seismicity behavior with creep may also be due to the change of aseismic loading after M2 for a single source. Aseismic loading has increased by a factor of 6 during the first few hours following stage A2 comparing to stage A1 as evidenced by the strain evolution following the initiation of each stage (Figure 5a). Hatakeyama et al. (2017) found change of loading rate has controlled the emergence and disappearance of REs following the 2011 M 9.0 Tohoku-oki earthquake.

As we cannot resolve the latter complexities, we constrain the aseismic moment magnitude of the afterslip during stage A2. This stage lasted about a month and produced large expansion at FBRB (see Figure 4b) that reached a level about 20 times larger than that during stage A1 (Figure 4a). Therefore, one may reasonably assume that stage A2 dominates the aseismic sequence and then controls its magnitude. Also, we use the dilatation value for stage A2 ($\sim 600 \text{ n}\epsilon$) as a proxy to estimate the amount of slip for different dimensions and locations of fault patches distributed along the CF. As evidenced by the dependence between afterslip and seismicity during the first 2 days of stage A2 (Figure 6), we expect afterslip to occur on the CF instead of on an adjacent fault. Note that slip direction is constrained to be similar to that of the mainshocks (about 80°). Since the slip amplitude of a source is “calibrated” from the strain change observation, we estimate the static surface displacements (using Okada, 1992) at the nearby GPS sites in order to identify sources undetected by GPS. Details about the approach are given in section S4 and are presented in Figure S10 in the supporting information.

We see that afterslip sources, undetected by GPS, are restricted to a small area (with dimensions of a few kilometers) located between depths of about 4 to 8 km on the northeastern termination of the CF. Kilometer-sized sources located near or within the area that encompasses the multiplets (about 6–7 km at depth, see Figure S10) have aseismic moment magnitude in the range of 4.6–4.9 and amplitudes of aseismic slip ranging from 10 cm to a few tens of centimeters. Larger sources (with dimensions of a few kilometers) show moment magnitude ranging from 4.6 to 5 and the maximal slip of a few centimeters. We thus believe that the source of stage A2 has the maximal dimensions of a few kilometers, is located at shallow depths (about 5 to 7 km), and characterized a geodetic moment magnitude of about 4.8 ± 0.2 .

5.4. Seismic-Aseismic Coupling on the CF

Each phase of afterslip follows a small-magnitude earthquake ($M_L < 5$) that occurred at shallow depths (< 8 km) on the CF, a continental thrust fault. Few examples of afterslip following moderate to large continental thrust earthquakes (Hsu et al., 2002, 2009; Jouanne et al., 2011) have been documented (Avouac, 2015). The mid-April 2010 sequence occurred in a small area that appears to characterize a low seismic activity during at least the past 20 years (see Figure 2a). The area is located at the updip limit of the large asperity (with dimensions of ~ 15 km \times 15 km) located at depths of 10–20 km that ruptured during the 2003 M_w 6.8 Chengkung earthquake (Thomas, Avouac, Champenois, et al., 2014). The coseismic slip failed to rupture the shallower creeping area at depths above 8–10 km, which experienced about a meter of postseismic slip during the 6–7 years following the Chengkung earthquake (Thomas, Avouac, Champenois, et al., 2014). Thus, the shallow northeastern section of the CF appears to have ruptured both seismically and aseismically during April 2010. Earthquake M1 could be a foreshock of M2. Stage A1 may have triggered M2 through positive Coulomb stress changes at the location of M2 hypocenter. Moreover, stage A2 may have triggered aftershock M3 through positive static stress changes during its early stage. Finally, aseismic creep may have been favored by the presence of the Lichi mélange in this part of the CF (Thomas, Avouac, Gratier, et al., 2014) as it presents a velocity-strengthening rheology.

The moment magnitude of afterslip is about 4.8 ± 0.2 that corresponds to a geodetic moment of $1 \times 10^{16} - 4 \times 10^{16}$ N m. The seismic moment of the sequence, computed with values inferred from Bayesian source inversions (see Table S3 for details), lies in the range of $6.4 \times 10^{15} - 9.5 \times 10^{15}$ N m. This corresponds to the maximal seismic moment magnitude of about 4.6. Although the ratio of the aseismic to seismic moment is difficult to accurately estimate due to the limitations described previously, we believe that the aseismic moment released by the afterslip is at least on the same order as the seismic moment of the sequence. This result is consistent with recent studies that show that the aseismic moment is comparable to (and even larger than) the seismic moment for small to moderate earthquakes ($M < 6$) (Fattahi et al., 2015; Gualandi et al., 2017; Hawthorne et al., 2016). Fattahi et al. (2015) proposed that the smaller the earthquake is, the larger is its aseismic contribution. Such a behavior is consistent with the predictions from rate-and-state friction laws; the ratio of aseismic to seismic moment is expected to increase if the size of the asperity decreases. Besides, the aseismic moment magnitude estimated here is smaller than that predicted by Ide et al. (2007) for a 1 month duration aseismic event (e.g., $M \sim 6$). The limited evidence of afterslip following small to moderate magnitude earthquakes can be mostly due to the resolution limits of geodetic sensors. The lower detection threshold for dilatometers and also the short distance between the sensor and the seismic sequence (about 6 km) have allowed us to detect afterslip signals. However, subtle crustal strain changes (with $M < 5$) associated with seismic swarms have also been detected by GPS (e.g., Gualandi et al., 2017), showing that the density of the GPS network is important for determining the detection threshold.

As shown in Figure 6, about 50% of the events of the sequence (22 events over 45) appear to be governed by slow shear failure during the first 2 days of stage A2. This is the first evidence for afterslip-driven aftershocks in the case of small-magnitude earthquakes ($M_w < 4.5 - 5.5$). Such a phenomenon has been evidenced by GPS signals during large earthquakes ($M_w \geq 7$) (see, for instance, Hsu et al., 2006; Perfettini & Avouac, 2004, 2007, or Jouanne et al., 2011) and also for dilatation signals during the 2003 M_8 Tokachi-oki earthquake (Takanami et al., 2013). In order to observe a potential link between slow creep and seismic energy released by the aftershocks, we also compared the afterslip evolution with the cumulative seismic moment during each phase but did not find a relevant correlation.

Further evidence for afterslip-driven aftershocks is the occurrence of a few multiplets near the mainshock area, especially during stage A1. Repeating aftershock clusters during the afterslip of the 2012 M_w 7.6 Nicoya earthquake were found around the epicenter region (Yao et al., 2017), for instance. Moreover, based on numerical

simulations and observations, one found that the features of REs (as recurrence interval and magnitude) are controlled by rate-and-state friction parameters (Chen & Lapusta, 2009; Chen et al., 2010) and that RE sequences interact predominantly through postseismic slip (Lui & Lapusta, 2016). We believe that afterslip following M1 (stage A1) would have changed the loading conditions of asperities on which ruptures have consequently been controlled by the rate friction parameters of the CF (see section 3.4).

Simultaneous observations of geodetic and seismic signatures of a transient crustal process are very rare. Studies have reported induced microseismicity due to aseismic slip associated with fluid injection (Guglielmi et al., 2015; Wei, Avouac, et al., 2015), aseismic transient-driven seismic swarms (e.g., Gualandi et al., 2017; Hirose et al., 2014; Lohman & McGuire, 2007; Roland & McGuire, 2009), or repeaters occurring simultaneously with transient slip (Bourouis & Bernard, 2007), but the details of the temporal evolution of the aseismic processes remain difficult to track (e.g., Gualandi et al., 2017). However, the absence of additional geodetic measurements and the limits of resolution for the microseismicity analysis strongly limit our ability to further interpret the link between seismic and aseismic processes during the sequence.

6. Conclusions

The study reports evidence for afterslip following a low-magnitude earthquake sequence ($M_L < 5$) on the CF, in southeast Taiwan. Afterslip, which occurred at shallow depths (< 8 km), is lasting about a month and characterized a cumulative geodetic moment magnitude of 4.8 ± 0.2 for a source with maximal dimensions of a few kilometers. The cumulative geodetic moment of the postseismic phase is at least equivalent to the coseismic moment of the sequence. Nevertheless, postseismic slip seems to control the repeated ruptures of small asperities during its first stage while the largest afterslip phase drives the rate of aftershocks during 2 days. Our study shows a rare case of seismic-aseismic coupling during a small-magnitude seismic sequence. Such observations remain rare for small earthquakes, mainly due to sensor limits in detecting the postseismic phase.

Acknowledgments

We thank Hugo Perfettini, two anonymous reviewers, and Associate Editor Emma Hill for their valuable comments allowing to improve the manuscript. We thank the support staff of the Carnegie Institution of Washington for the construction, installation, and maintenance of the dilatometers. We are grateful to many colleagues at the Institute of Earth Sciences, Academia Sinica who have participated in collecting strainmeter data. We thank Jian-Cheng Lee and Chung-Hsiang Mu for their useful details about the Chihshang Fault geology. We thank Wen-Tzong Liang and Wen-Hui Lee for providing the seismological data. Some figures were drawn using the General Mapping Tools (Wessel & Smith, 1998). Strainmeter and GPS data are available at dmc.earth.sinica.edu.tw. Broadband seismological data are available at gdms.cwb.gov.tw (CWB data) and at bats.earth.sinica.edu.tw (BATS data) (Institute of Earth Sciences, Academia Sinica, Taiwan, 1996). This work was supported by the Academia Sinica and the Ministry of Science and Technology of the Republic of China grant MOST 104-2628-M-001-008-MY4. This is the contribution of the Institute of Earth Sciences, Academia Sinica, IESAS2232.

References

- Altamini, Z., Collilieux, X., Legrand, J., Garayt, B., & Boucher, C. (2007). ITRF2005: A new release of the International Terrestrial Reference Frame based on time series of station positions and Earth orientation parameters. *Journal of Geophysical Research*, 112, B09401. <https://doi.org/10.1029/2007JB004949>
- Angelier, J., Chu, H. T., Lee, J. C., & Hu, J. C. (2000). Active faulting and earthquake risk: The Chihshang Fault case, Taiwan. *Journal of Geodynamics*, 29, 151–185.
- Avouac, J. P. (2015). From geodetic imaging of seismic and aseismic fault slip to dynamic modeling of the seismic cycle. *Annual Review of Earth and Planetary Sciences*, 43, 233–271.
- Barnhart, W. D., & Lohman, R. B. (2013). Phantom earthquakes and triggered aseismic creep: Vertical partitioning of strain during earthquake sequences in Iran. *Geophysical Research Letters*, 40, 819–823. <https://doi.org/10.1002/grl.50201>
- Barrier, E., & Angelier, J. (1986). Active collision in eastern Taiwan: The coastal range. *Tectonophysics*, 125, 39–72.
- Beeler, N. M., Lockner, D. A., & Hickman, S. H. (2001). A simple stick-slip and creep slip model for repeating earthquakes and its implication for micro-earthquakes at Parkfield. *Bulletin of the Seismological Society of America*, 91, 1797–1804.
- Bell, J. W., Amelung, F., & Henry, C. D. (2012). InSAR analysis of the 2008 Reno-Mogul earthquake swarm: Evidence for westward migration of Walker Lane style dextral faulting. *Geophysical Research Letters*, 39, L18306. <https://doi.org/10.1029/2012GL052795>
- Bourouis, S., & Bernard, P. (2007). Evidence for coupled seismic and aseismic fault slip during water injection in the geothermal site of Soultz (France), and implications for seismogenic transients. *Geophysical Journal International*, 69, 723–732.
- Brune, J. N. (1970). Tectonic stress and the spectra of seismic shear waves from earthquakes. *Journal of Geophysical Research*, 75(26), 4997–5009.
- Bürgmann, R., Ergintav, S., Segall, P., Hearn, E. H., McClusky, S., Reilinger, R. E., et al. (2002). Time-space variable afterslip on and deep below the Izmit earthquake rupture. *Bulletin of the Seismological Society of America*, 92, 138–160.
- Canitano, A., Bernard, P., Linde, A. T., & Sacks, S. (2013). Analysis of signals of a borehole strainmeter in the western rift of Corinth, Greece. *Journal of Geodetic Science*, 3(1), 63–76.
- Canitano, A., Bernard, P., Linde, A. T., Sacks, S., & Boudin, F. (2014). Correcting high-resolution borehole strainmeter data from complex external influences and partial-solid coupling: The case of Trizonia, rift of Corinth (Greece). *Pure and Applied Geophysics*, 171(8), 1759–1790.
- Canitano, A., Hsu, Y. J., Lee, H. M., Linde, A. T., & Sacks, S. (2015). Near-field strain observations of the October 2013 Ruisui, Taiwan, earthquake: Source parameters and limits of very short-term strain detection. *Earth Planets Space*, 67, 125. <https://doi.org/10.1186/s40623-015-0284-1>
- Canitano, A., Hsu, Y. J., Lee, H. M., Linde, A. T., & Sacks, S. (2017). A first modeling of dynamic and static crustal strain field from near-field dilatation measurements: Example of the 2013 M_w 6.2 Ruisui earthquake, Taiwan. *Journal of Geodesy*, 91(1), 1–8.
- Canitano, A., Hsu, Y. J., Lee, H. M., Linde, A. T., & Sacks, S. (2018). Calibration for the shear strain of 3-component borehole strainmeters in eastern Taiwan through Earth and ocean tidal waveform modeling. *Journal of Geodesy*, 92(3), 223–240. <https://doi.org/10.1007/s00190-017-1056-4>
- Chai, B. H. (1972). Structure and tectonic evolution of Taiwan. *American Journal of Science*, 272, 383–432.
- Champenois, J., Fruneau, B., Pathier, E., Deffontaines, B., Lin, K. C., & Hu, J. C. (2012). Monitoring of active tectonic deformations in the Longitudinal Valley (Eastern Taiwan) using persistent scatterer InSAR method with ALOS PALSAR data. *Earth and Planetary Science Letters*, 337–338, 144–155.

- Chen, K. H., Toda, S., & Rau, R. J. (2008). A leaping, triggered sequence along a segmented fault: The 1951 M_L 7.3 Hualien-Taitung earthquake sequence in eastern Taiwan. *Journal of Geophysical Research*, *113*, B02304. <https://doi.org/10.1029/2007JB005048>
- Chen, K. H., Nadeau, R. M., & Rau, R. J. (2008). Characteristic repeating earthquakes in an arc-continent collision boundary zone: The Chihshang Fault of eastern Taiwan. *Earth and Planetary Science Letters*, *276*, 262–272.
- Chen, T., & Lapusta, N. (2009). Scaling of small repeating earthquakes explained by interaction of seismic and aseismic slip in a rate and state fault model. *Journal of Geophysical Research*, *114*, B01311. <https://doi.org/10.1029/2008JB005749>
- Chen, K. H., Rau, R. J., & Hu, J. C. (2009). Variability of repeating earthquake behavior along the Longitudinal Valley fault zone of eastern Taiwan. *Journal of Geophysical Research*, *114*, B05306. <https://doi.org/10.1029/2007JB005518>
- Chen, K. H., Bürgmann, R., Nadeau, R. M., Chen, T., & Lapusta, N. (2010). Postseismic variation in seismic moment and recurrence interval of repeating earthquakes. *Earth and Planetary Science Letters*, *299*, 118–125.
- Ching, K. E., Rau, R. J., & Zeng, Y. (2007). Coseismic source model of the 2003 M_w 6.8 Chengkung earthquake, Taiwan, determined from GPS measurements. *Journal of Geophysical Research*, *112*, B06422. <https://doi.org/10.1029/2006JB004439>
- D'Agostino, N., Cheloni, D., Fornaro, G., Giuliani, R., & Reale, D. (2012). Space-time distribution of afterslip following the 2009 L'Aquila earthquake. *Journal of Geophysical Research*, *117*, B02402. <https://doi.org/10.1029/2011JB008523>
- Dominguez, L. A., Taira, T., & Santoyo, M. A. (2016). Spatiotemporal variations of characteristic repeating earthquake sequences along the Middle America Trench in Mexico. *Journal of Geophysical Research: Solid Earth*, *121*, 8855–8870. <https://doi.org/10.1002/2016JB013242>
- Fattahi, H., Amelung, F., Chaussard, E., & Wdowinski, S. (2015). Coseismic and postseismic deformation due to the 2007 M5.5 Ghazaband fault earthquake, Balochistan, Pakistan. *Geophysical Research Letters*, *42*, 3305–3312. <https://doi.org/10.1002/2015GL063686>
- Freed, A. M. (2007). Afterslip (and only afterslip) following the 2004 Parkfield, California, earthquake. *Geophysical Research Letters*, *34*, L06312. <https://doi.org/10.1029/2006GL029155>
- Furuya, M., & Satyabala, S. P. (2008). Slow earthquake in Afghanistan detected by InSAR. *Geophysical Research Letters*, *35*, L06309. <https://doi.org/10.1029/2007GL033049>
- Godano, M., Bernard, P., & Dublanchet, P. (2015). Bayesian inversion of seismic spectral ratio for source scaling. Application to a persistent multiplet in the Western Corinth rift. *Geophysical Research Letters*, *120*, 7683–7712. <https://doi.org/10.1002/2015JB012217>
- Gualandi, A., Nichele, C., Serpelloni, E., Chiaraluce, L., Latorre, D., Belardinelli, M. E., & Avouac, J. P. (2017). Aseismic deformation associated with an earthquake swarm in the northern Apennines (Italy). *Geophysical Research Letters*, *42*, 7706–7714. <https://doi.org/10.1002/2017GL073687>
- Guglielmi, Y., Cappa, F., Avouac, J. P., Henry, P., & Elsworth, D. (2015). Seismicity triggered by fluid injection-induced aseismic slip. *Science*, *348*(6240), 1224–1226.
- Hart, R. H. G., Gladwin, M. T., Gwyther, R. L., Agnew, D. C., & Wyatt, F. K. (1996). Tidal calibration of borehole strainmeters: Removing the effects of local inhomogeneity. *Journal of Geophysical Research*, *101*, 25,553–25,571.
- Hatakeyama, N., Uchida, N., Matsuzawa, T., & Nakamura, W. (2017). Emergence and disappearance of interplate repeating earthquakes following the 2011 $M9.0$ Tohoku-oki earthquake: Slip behavior transition between seismic and aseismic depending on the loading rate. *Journal of Geophysical Research*, *122*, 5160–5180. <https://doi.org/10.1002/2016JB013914>
- Hawthorne, J. C., Simons, M., & Ampuero, J.-P. (2016). Estimates of aseismic slip associated with small earthquakes near San Juan Bautista, CA. *Journal of Geophysical Research: Solid Earth*, *121*, 8254–8275. <https://doi.org/10.1002/2016JB013120>
- Herring, T., King, W., & McCluskey, S. M. (2010). *Introduction to GAMIT/GLOBK release 10.4*. Cambridge: Massachusetts Institute of Technology.
- Hirose, H., Matsuzawa, T., Kimura, T., & Kimura, H. (2014). The Boso slow slip events in 2007 and 2011 as a driving process for the accompanying earthquake swarm. *Geophysical Research Letters*, *41*, 2778–2885. <https://doi.org/10.1002/2014GL059791>
- Hsu, Y. J., Bechor, N., Segall, P., Yu, S. B., Kuo, L. C., & Ma, K. F. (2002). Rapid afterslip following the 1999 Chi-Chi, Taiwan earthquake. *Geophysical Research Letters*, *29*, 1–4. <https://doi.org/10.1029/2002GL014967>
- Hsu, Y. J., Simons, M., Avouac, J. P., Galetzka, J., Sieh, K., Chlieh, M., et al. (2006). Frictional afterslip following the 2005 Nias-Simeulue earthquake, Sumatra. *Science*, *312*, 1921–1926.
- Hsu, Y. J., Segall, P., Yu, S. B., Kuo, L. C., & Williams, C. A. (2007). Temporal and spatial variations of post-seismic deformation following the 1999 Chi-Chi, Taiwan earthquake. *Geophysical Journal International*, *169*, 367–379.
- Hsu, Y. J., Yu, S. B., & Chen, H. Y. (2009). Coseismic and postseismic deformation associated with the 2003 Chengkung, Taiwan, earthquake. *Geophysical Journal International*, *176*, 420–430.
- Hsu, Y. J., Ando, M., Yu, S. B., & Simons, M. (2012). The potential for a great earthquake along the southernmost Ryukyu subduction zone. *Geophysical Research Letters*, *39*, L14302. <https://doi.org/10.1029/2012GL052764>
- Hsu, Y. J., Chang, Y. S., Liu, C. C., Lee, H. M., Linde, A. T., Sacks, S., et al. (2015). Revisiting borehole strain, typhoons, and slow earthquakes using quantitative estimates of precipitation-induced strain changes. *Journal of Geophysical Research: Solid Earth*, *120*, 4556–4571. <https://doi.org/10.1002/2014JB011807>
- Ide, S., Beroza, G. C., Shelly, D. R., & Uchida, T. (2007). A scaling law for slow earthquakes. *Nature*, *447*, 76–79.
- Igarashi, T., Matsuzawa, T., & Hasegawa, A. (2003). Repeating earthquakes and interplate aseismic slip in the northeastern Japan subduction zone. *Journal of Geophysical Research*, *108*(B5), 2249. <https://doi.org/10.1029/2002JB001920>
- Institute of Earth Sciences, Academia Sinica, Taiwan (1996). Broadband array in Taiwan for seismology, Institute of Earth Sciences, Academia Sinica, Taiwan. Other/Seismic Network. <https://doi.org/10.7914/SN/TW>
- Johanson, I. A., & Bürgmann, R. (2010). Coseismic and postseismic slip from the 2003 San Simeon earthquake and their effects on backthrust slip and the 2004 Parkfield earthquake. *Journal of Geophysical Research*, *115*, B07411. <https://doi.org/10.1029/2009JB006599>
- Johnson, K. M., Bürgmann, R., & Larson, K. (2006). Frictional properties on the San Andreas fault near Parkfield, California, inferred from models of afterslip following the 2004 earthquake. *Bulletin of the Seismological Society of America*, *96*, 321–338.
- Jouanne, F., Awan, A., Madji, A., Pêcher, A., Latif, M., Kausar, A., et al. (2011). Postseismic deformation in Pakistan after the 8 October 2005 earthquake: Evidence of afterslip along a flat north of the Balakot-Bagh thrust. *Journal of Geophysical Research*, *116*, B07401. <https://doi.org/10.1029/2010JB007903>
- Kanamori, H., & Anderson, D. L. (1975). Theoretical basis of some empirical relations in seismology. *Bulletin of the Seismological Society of America*, *65*(5), 1073–1095.
- Kato, A., Fukuda, J., Kumazawa, T., & Nakagawa, S. (2016). Accelerated nucleation of the 2014 Iquique, Chile M_w 8.2 earthquake. *Scientific Reports*, *6*, 24792. <https://doi.org/10.1038/srep24792>
- Kuo, H., Wu, Y. M., Chang, C. H., Hu, J. C., & Chen, W. S. (2004). Relocation of eastern Taiwan earthquakes and tectonic implications. *Terrestrial, Atmospheric and Oceanic Sciences*, *15*, 647–666.
- Langbein, J., Murray, J. R., & Snyder, H. A. (2006). Coseismic and initial postseismic deformation from the 2004 Parkfield, California, earthquake, observed by Global Positioning System, electronic distance meter, creepmeters, and borehole strainmeters. *Bulletin of the Seismological Society of America*, *96*(4B), S304–S320.

- Lee, J. C., Angelier, J., Chu, H. T., Hu, J. C., & Jeng, F. S. (2001). Continuous monitoring of an active fault in a plate suture zone: A creepmeter study of the Chihshang Fault, eastern Taiwan. *Tectonophysics*, 332(1–2), 219–240.
- Lee, J. C., Angelier, J., Chu, H. T., Hu, J. C., Jeng, F., & Rau, R. J. (2003). Active fault creep variations at Chihshang, Taiwan, revealed by creep meter monitoring, 1998–2001. *Journal of Geophysical Research*, 108(B11), 2528. <https://doi.org/10.1029/2003JB002394>
- Lee, J. C., Chu, H. T., Angelier, J., Hu, J. C., Chen, H. Y., & Yu, S. B. (2006). Quantitative analysis of surface coseismic faulting and postseismic creep accompanying the 2003, $M_w = 6.5$, Chengkung earthquake in eastern Taiwan. *Journal of Geophysical Research*, 111, B02405. <https://doi.org/10.1029/2005JB003612>
- Leongline, O., & Marsan, D. (2009). Inferring the coseismic and postseismic stress changes caused by the 2004 $M_w = 6$ Parkfield earthquake from variations of recurrence times of microearthquakes. *Journal of Geophysical Research*, 114, B10303. <https://doi.org/10.1029/2008JB006118>
- Lin, J., & Stein, R. S. (2004). Stress triggering in thrust and subduction earthquakes and stress interaction between the southern San Andreas and nearby thrust and strike-slip faults. *Journal of Geophysical Research*, 109, B02303. <https://doi.org/10.1029/2003JB002607>
- Liu, C. C., Linde, A. T., & Sacks, I. S. (2009). Slow earthquakes triggered by typhoons. *Nature*, 459, 833–836.
- Lohman, R. B., & McGuire, J. J. (2007). Earthquake swarms driven by aseismic creep in the Salton Trough, California. *Journal of Geophysical Research*, 112, B04405. <https://doi.org/10.1029/2006JB004596>
- Lui, S. K. Y., & Lapusta, N. (2016). Repeating microearthquake sequences interact predominantly through postseismic slip. *Nature Communications*, 7, 13020. <https://doi.org/10.1038/ncomms13020>
- Madariaga, R. (1976). Dynamics of an expanding circular fault. *Bulletin of the Seismological Society of America*, 66(3), 639–666.
- Mahsas, A., Lammali, K., Yelles, K., Calais, E., Freed, A. M., & Briole, P. (2008). Shallow afterslip following the 2003 May 21, $M_w = 6.9$ Boumerdes earthquake, Algeria. *Geophysical Journal International*, 172, 155–166. <https://doi.org/10.1111/j.1365-246X.2007.03594.x>
- Marone, C. J., Scholz, C. H., & Bilham, R. (1991). On the mechanics of earthquake afterslip. *Journal of Geophysical Research*, 96(B11), 8441–8452.
- Mavrommatis, A., Segall, P., Uchida, N., & Johnson, K. (2015). Long-term acceleration of aseismic slip preceding the M_w 9 Tohoku-oki earthquake: Constraints from repeating earthquakes. *Geophysical Research Letters*, 42, 9717–9725. <https://doi.org/10.1002/2015GL066069>
- Mendoza, C., & Hartzell, S. H. (1988). Aftershock properties and main shock faulting. *Bulletin of the Seismological Society of America*, 78(4), 1438–1449.
- Mignan, A., Werner, M. J., Wiemer, S., Liu, C. C., & Wu, Y. M. (2011). Bayesian estimation of the spatially varying completeness magnitude of earthquake catalogs. *Bulletin of the Seismological Society of America*, 101(3), 1371–1385.
- Mouyen, M., Canitano, A., Chao, B. F., Hsu, Y. J., Steer, P., Longuevergne, L., & Boy, J. P. (2017). Typhoon-induced ground deformation. *Geophysical Research Letters*, 44, 11,004–11,011. <https://doi.org/10.1002/2017GL075615>
- Nadeau, R. M., & Johnson, L. R. (1998). Seismological studies at Parkfield VI: Moment release rates and estimates of source parameters for small repeating earthquakes. *Bulletin of the Seismological Society of America*, 88(3), 790–814.
- Nadeau, R. M., & McEvilly, T. V. (1999). Fault slip rates at depth from recurrence intervals of repeating microearthquakes. *Science*, 285(5428), 718–721.
- Okada, Y. (1992). Internal deformation due to shear and tensile faults in a half-space. *Bulletin of the Seismological Society of America*, 82(2), 1018–1040.
- Perfettini, H., & Avouac, J. P. (2004). Postseismic relaxation driven by brittle creep: A possible mechanism to reconcile geodetic measurements and the decay rate of aftershocks, application to the Chi-Chi earthquake, Taiwan. *Journal of Geophysical Research*, 109, B02304. <https://doi.org/10.1029/2003JB002488>
- Perfettini, H., Avouac, J. P., & Ruegg, J. C. (2005). Geodetic displacements and aftershocks following the 2001 $M_w = 8.4$ Peru earthquake: Implications for the mechanics of the earthquake cycle along subduction zones. *Journal of Geophysical Research*, 110, B09404. <https://doi.org/10.1029/2004JB003522>
- Perfettini, H., & Avouac, J. P. (2007). Modeling afterslip and aftershocks following the 1992 Landers earthquake. *Journal of Geophysical Research*, 112, B07409. <https://doi.org/10.1029/2006JB004399>
- Roland, E., & McGuire, J. J. (2009). Earthquake swarms on transform faults. *Geophysical Journal International*, 178, 1677–1690.
- Ruiz, S., Aden-Antoniow, F., Baez, J. C., Otarola, C., Potin, B., del Campo, F., et al. (2017). Nucleation phase and dynamic inversion of the M_w 6.9 Valparaíso 2017 earthquake in Central Chile. *Geophysical Research Letters*, 44, 10,290–10,297. <https://doi.org/10.1002/2017GL075675>
- Sacks, S., Suyehiro, S., Evertson, D. W., & Yamagishi, Y. (1971). Sacks-Evertson strainmeter, its installation in Japan and some preliminary results concerning strain steps. *Papers in Meteorology and Geophysics*, 22, 195–208.
- Schaff, D. P., Beroza, G. C., & Shaw, B. E. (1998). Postseismic response of repeating aftershocks. *Geophysical Research Letters*, 25(24), 4549–4552.
- Shyu, J. B. H., Sieh, K., Chen, Y. G., & Liu, C. S. (2005). Neotectonic architecture of Taiwan and its implications for future large earthquakes. *Journal of Geophysical Research*, 110, B08401. <https://doi.org/10.1029/2004JB003251>
- Taira, T., Bürgmann, R., Nadeau, R. M., & Dreger, D. S. (2014). Variability of fault slip behavior along the San Andreas Fault in the San Juan Bautista region. *Journal of Geophysical Research: Solid Earth*, 119, 8827–8844. <https://doi.org/10.1002/2014JB011427>
- Takai, K., Kumagai, H., & Fujii, N. (1999). Evidence for slow slip following a moderate-size earthquake (m_w 5.7) in a subducting plate. *Geophysical Research Letters*, 26(40), 2113–2116.
- Takanami, T., Linde, A. T., Sacks, S. I., Kitagawa, G., & Peng, H. (2013). Modeling of the post-seismic slip of the 2003 Tokachi-oki earthquake M 8 off Hokkaido: Constraints from volumetric strain. *Earth Planets Space*, 65(7), 731–738.
- Thomas, M. Y., Avouac, J. P., Champenois, J., Lee, J. C., & Kuo, L. C. (2014). Spatiotemporal evolution of seismic and aseismic slip on the Longitudinal Valley fault, Taiwan. *Journal of Geophysical Research: Solid Earth*, 119, 5114–5139. <https://doi.org/10.1002/2013JB010603>
- Thomas, M. Y., Avouac, J. P., Gratier, J. P., & Lee, J. C. (2014). Lithologic control on the deformation mechanism and the mode of fault slip on the Longitudinal Valley fault, Taiwan. *Tectonophysics*, 632, 48–63.
- Toda, S., Stein, R. S., Richards-Dinger, K., & Bozkurt, S. (2005). Forecasting the evolution of seismicity in southern California: Animations built on earthquake stress transfer. *Journal of Geophysical Research*, 110, B05S16. <https://doi.org/10.1029/2004JB003415>
- Turner, R. C., Nadeau, R. M., & Bürgmann, R. (2013). Aseismic slip and fault interaction from repeating earthquakes in the Loma Prieta aftershock zone. *Geophysical Research Letters*, 40, 1079–1083. <https://doi.org/10.1002/grl.50212>
- Uchida, N., Matsuzawa, T., Hasegawa, A., & Igarashi, T. (2003). Interplate quasi-static slip off Sanriku, NE Japan, estimated from repeating earthquakes. *Geophysical Research Letters*, 30(15), 1801. <https://doi.org/10.1029/2003GL017452>

- Uchida, N., Shimamura, K., Matsuzawa, T., & Okada, T. (2015). Postseismic response of repeating earthquakes around the 2011 Tohoku-oki earthquake: Moment increases due to the fast loading. *Journal of Geophysical Research: Solid Earth*, *120*, 259–274. <https://doi.org/10.1002/2013JB010933>
- Vidale, J. E., Ellsworth, W. L., Cole, A., & Marone, C. (1994). Variations in rupture process with recurrence interval in a repeated small earthquake. *Nature*, *368*, 624–626. <https://doi.org/10.1038/368624a0>
- Waldhauser, F., & Ellsworth, W. L. (2000). A double-difference earthquake location algorithm: Method and application to the northern Hayward fault. *Bulletin of the Seismological Society of America*, *90*(6), 1353–1368.
- Wei, S., Barbot, S., Graves, R., Lienkaemper, J. J., Wang, T., Hudnut, K., et al. (2015). The 2014 M_w 6.1 South Napa earthquake: A unilateral rupture with shallow asperity and rapid afterslip. *Seismological Research Letters*, *86*(2A), 344–354. <https://doi.org/10.1785/0220140249>
- Wei, S., Avouac, J. P., Hudnut, K. W., Donnellan, A., Parker, J. W., Graves, R. W., et al. (2015). The 2012 Brawley swarm triggered by injection-induced aseismic slip. *Earth and Planetary Science Letters*, *422*, 115–125.
- Wells, D. L., & Coppersmith, K. J. (1994). New empirical relationships among magnitude, rupture length, rupture width, rupture area, and surface displacement. *Bulletin of the Seismological Society of America*, *84*(4), 974–1002.
- Wenzel, H. (1995). The nanogal software: Earth tide data processing package ETERNA 3.30. *Bulletin d'Informations Mareés Terrestres*, *124*, 9425–9439.
- Wessel, P., & Smith, W. H. F. (1998). New, improved version of the Generic Mapping Tools released. *Eos, Transactions American Geophysical Union*, *79*, 579. <https://doi.org/10.1029/98EO00426>
- Yang, H., Zhu, L., & Chu, R. (2009). Fault-plane determination of the 18 April 2008 Mount Carmel, Illinois, earthquake by detecting and relocating aftershocks. *Bulletin of the Seismological Society of America*, *99*(6), 3413–3420.
- Yao, D., Walter, J. I., Meng, X., Hobbs, T. E., Peng, Z., Newman, A. V., et al. (2017). Detailed spatiotemporal evolution of microseismicity and repeating earthquakes following the 2012 M_w 7.6 Nicoya earthquake. *Journal of Geophysical Research: Solid Earth*, *122*, 524–542. <https://doi.org/10.1002/2016JB013632>
- Yu, S. B., & Liu, C. C. (1989). Fault creep on the central segment of the Longitudinal Valley fault, eastern Taiwan. *Journal of the Geological Society of China*, *32*, 209–231.
- Yu, S. B., Chen, H. Y., & Kuo, L. C. (1997). Velocity field of GPS stations in the Taiwan area. *Tectonophysics*, *274*, 41–59.
- Yu, S. B., Kuo, L. C., Punongbayan, R., & Ramos, E. G. (1999). GPS observation of crustal deformation in the Taiwan-Luzon region. *Geophysical Research Letters*, *26*, 923–926.
- Yu, S. B., & Kuo, L. C. (2001). Present-day crustal motion along the Longitudinal Valley fault, eastern Taiwan. *Tectonophysics*, *333*, 199–217.